Mon. Not. R. Astron. Soc. **000**, 1–21 (2014) Printed 12 August 2014 (MN LATEX style file v2.2)

Probing large scale filaments with H I and ^{3}He II

Yoshitaka Takeuchi[1⋆], Saleem Zaroubi[2] and Naoshi Sugiyama[1,3,4]

[1] *Department of physics, Nagoya University, Naogya 464-8602, Japan*
[2] *Kapteyn Astronomical Institute, University of Groningen, P.O. Box 800, 9700 AV Groningen, The Netherlands*
[3] *Kobayashi-Maskawa Institute, Nagoya University, Nagoya 464-8602, Japan*
[4] *Kavli Institute for the Physics and Mathematics of the Universe, University of Tokyo, Kashiwa 277-8568, Japan*

arXiv:1408.2450v1 [astro-ph.CO] 11 Aug 2014

Accepted, Received; in original form

ABSTRACT

We explore the observability of the neutral hydrogen (H I) and the singly-ionized isotope helium-3 (^{3}He II) in the intergalactic medium (IGM) from the Epoch of Reionization down to the local Universe. The hyperfine transition of ^{3}He II, which is not as well known as the H I transition, has energy splitting corresponding to 8 cm. It also has a larger spontaneous decay rate than that of neutral hydrogen, whereas its primordial abundance is much smaller. Although both species are mostly ionized in the IGM, the balance between ionization and recombination in moderately high density regions renders them abundant enough to be observed. We estimate the emission signal of both hyperfine transitions from large scale filamentary structures and discuss the prospects for observing them with current and future radio telescopes. We conclude that H I in filaments is possibly observable even with current telescopes after 100 hours of observation. On the other hand, ^{3}He II is only detectable with future telescopes, such as SKA, after the same amount of time.

Key words: hyperfine structure, hydrogen, helium-3, radio astronomy, cosmology: large-scale structure of Universe

1 INTRODUCTION

Since the prediction of the 21 cm hyperfine transition by van de Hulst (1945) and its first detection by Ewen & Purcell (1951) and Muller & Oort (1951), forbidden quantum transition lines have been powerful tools in exploring various astrophysical systems. The advent of new larger and more sensitive radio telescopes makes it possible to use such tools for exploring even higher redshifts and lower density environments. Two recent examples are the use of redshifted 21 cm for exploring the Epoch of Reionization (EoR) (see e.g., Furlanetto et al. (2006); Pritchard & Loeb (2012); Zaroubi (2013)); and for mapping neutral gas around redshift $\sim$ 1-2 to probe the baryon acoustic peaks (Chang et al. 2008). Another line, that has been discussed in the literature, is the singly-ionized helium-3 isotope, ^{3}He II (Townes 1957; Sunyaev 1966; Goldwire & Goss 1967; Rood et al. 1979; Bell 2000; McQuinn & Switzer 2009; Bagla & Loeb 2009). In this study we propose to use H I and ^{3}He II to detect large scale filaments and the accumulation of baryons within them as a function of redshift.

At the local Universe, most of the baryons in the intergalactic space reside in filamentary structures, the so-called cosmic web (Bond et al. 1996). These filaments are readily seen by modern galaxy surveys, such as the 2-degree Field Galaxy Redshift Survey (Colless et al. 2001; Erdoğdu et al. 2004), the Sloan Digital Sky Survey (York et al. 2000) and the 2-Micron All-Sky Survey (Skrutskie et al. 2006). Unfortunately, however, such surveys are not able to probe the baryonic content of these filaments and its distribution, where less than half of baryons at the local Universe have been identified (Cen & Ostriker 1999; Fukugita & Peebles 2004).

The observation of filamentary structures in the IGM through the hyperfine transition of neutral hydrogen can be a powerful tool that has the potential for detecting the missing baryons in the local Universe (see e.g., Popping et al. (2009) and

⋆ E-mail:yoshitaka@nagoya-u.jp

Popping & Braun (2011)). However, below redshift ~ 6, the detection of H I in the diffuse IGM becomes very difficult as the Universe reionizes and a very small neutral fraction is left. Despite this difficulty, Chang et al. (2010) and Masui et al. (2012) have detected H I at low redshift by cross correlating the aggregate 21-cm glow with data from other probes of large-scale structure. Still, the signal of the auto-correlation at low-redshifts can be interpreted as an upper bound on the 21 cm signal (Switzer et al. 2013). Direct detection of H I emission signal from IGM filaments has not been reported yet, but Ly-α forest absorption towards background quasars implies H I from filaments.

Observation of ^{3}He II transition from the diffuse and filamentary structure in the IGM is very difficult to carry out, mainly because of its low abundance relative to hydrogen, and therefore, in principle in harder to detect. Furthermore, the sensitivity of the current radio telescopes at the appropriate frequency range is too poor for such a task. However, despite the low primordial abundance of ^{3}He relative to hydrogen ($\sim 10^{-5}$), it has some mitigating factors that render it observationally accessible. These factors are as follows:

(i) The spontaneous decay rate of ^{3}He II ($A_{10} = 1.959 \times 10^{-12}$ s^{-1}) is $\sim$680 times larger than that of the H I ($A_{10} = 2.876 \times 10^{-15}$ s^{-1}) (Gould 1994; Sunyaev 1966; Goldwire & Goss 1967), which significantly increases its emission rate.

(ii) The ionization energy of He II (54.4 eV) is 4 times larger than that of neutral hydrogen (13.6 eV), namely, it requires harder photons to fully ionize. Conversely, this difference in ionization energy causes the He III recombination rate to be $\sim$5 times larger than that of H II (Verner & Ferland 1996). Hence, the abundance fraction of ^{3}He II in the IGM should be larger than that of H I.

(iii) The line transition occurs at a frequency of 8.7 GHz, in which the foreground synchrotron radiation from our galaxy and distortions from the terrestrial ionosphere are both less pronounced.

The overdensity of filaments in the IGM is roughly of the order of 10-100 times the mean density of the Universe. Therefore, given the size of such filaments, one can accumulate a sizable column density of both H I and ^{3}He II, in particular if they are elongated along the line of sight. Furthermore, at these densities, the recombination rates for both species are generally shorter than Hubble time and a reasonable fraction of H I and He II is expected to be present. Detection of either species will go a long way in accounting for the baryons in the Universe at the redshift of detection. In addition, the relative abundance of these species can constrain the hardness of the UV background as a function of redshift.

Our aim in this study is to estimate the prospect of observing these two species within large scale structure filaments with the present and future radio telescopes in the redshift range $\sim 0-8$. Here, we consider a number of single dish telescopes, e.g., GBT[1] (Chang et al. 2010; Masui et al. 2012) and Arecibo[2](Freudling et al. 2011), and radio interferometers such as EVLA[3], and GMRT[4]. Note that LOFAR does not have the proper frequency range for observing either of the two transitions, except H I at $z \gtrsim 6$ (van Haarlem et al. 2013). We also make predictions for future telescopes that generally have more sensitivity, a larger field of view and wider frequency coverage: FAST[5], MeerKAT[6] and, of course, the mega radio telescope SKA[7], which is expected to be completed around 2024.

This paper is organized as follow. We summarize the physical models used in the paper for calculating the H I and ^{3}He II signal from large scale filamentary structure in the IGM in Section 2. In the same section, we also evaluate the abundance of each ionization state, the gas temperature in the IGM and the spin and brightness temperatures. The predicted hyperfine transition signal of H I and ^{3}He II for simple models as well as for filaments from large scale structure simulations is presented in Section 3. Finally we discuss the prospects of observing the emission signal of the hyperfine transition from filamentary structures with current and future radio telescopes in Section 4.2. The paper ends with a conclusion and discussion section.

Throughout this paper, we adopt the cosmological parameters from the WMAP 7 years data (Komatsu et al. 2011).

2 THE PHYSICAL MODEL FOR H I AND ^{3}He II

To calculate the signal of H I and ^{3}He II, an evaluation of their ionization states and abundances is required. To achieve this, we solve the radiation balance equations between the ionization and recombination processes. These processes are highly dependent on the environment in the IGM, e.g. the density and the temperature of gas. The photo-ionization and the heating processes through the IGM are also determined by the background radiation field. The UV/X-ray background model adopted in this paper is the Haardt & Madau (2012, hereafter HM12) model.

The observed signal of the hyperfine transition is related to the relative occupation number of the excited state relative to

[1] https://science.nrao.edu/facilities/gbt
[2] http://www.naic.edu/
[3] https://science.nrao.edu/facilities/vla
[4] http://gmrt.ncra.tifr.res.in/
[5] http://fast.bao.ac.cn/en/FAST.html
[6] http://www.ska.ac.za/meerkat/index.php
[7] http://www.skatelescope.org/

the ground state, which determines the spin temperature. Other than the CMB, two processes affect the relative occupation number density of hyperfine state: the collisional excitation process and the Ly-α pumping of the line, also known as the Wouthuysen-Field process (Wouthuysen 1952; Field 1958, 1959). We estimate the spin temperature taking into account both these processes.

In this section, the physical equations needed for the estimation of the hyperfine transition are summarize and the signal expected from a simple slab model that represents the filamentary structure in the IGM is calculated. Specifically, in Subsec. 2.1 and 2.2, we calculate the evolution of the abundance for each ionization state and the gas temperature in the IGM following the equations in Fukugita & Kawasaki (1994), where we adopt the photo-ionization rate $\Gamma(z)$ and the heating function $\mathcal{H}(z)$ given by HM12. In Subsec. 2.3, the physical processes determining the spin state and estimate the spin temperature are summarized. Finally, the brightness temperature expected from a simple filamentary structure model is shown in subsec. 2.4.

2.1 Ionization state of hydrogen and helium

We here assume that the system contains only H and He. The abundances of each H and He species, i.e., H I, H II, He I, He II and He III, are given by solving the balance equation between the ionization and recombination processes (Fukugita & Kawasaki 1994). The equation for the hydrogen species is:

$$\frac{d}{dt}\left[\frac{n_{\rm HII}}{n_{\rm H}}\right] = \Gamma_{\rm HI} n_e \frac{n_{\rm HI}}{n_{\rm H}} + \beta_{\rm HI} n_e \frac{n_{\rm HI}}{n_{\rm H}} - \alpha_{\rm HII} n_e \frac{n_{\rm HII}}{n_{\rm H}}\,, \tag{1}$$

where n_e is the number density of electron, $n_{\rm HI}$ and $n_{\rm HII}$ are respectively the number densities of the neutral and the ionized hydrogen, and $n_{\rm H} \equiv n_{\rm HI} + n_{\rm HII}$ is the total number density of hydrogen.

The balance equations for He I, He II and He III are:

$$\frac{d}{dt}\left[\frac{n_{\rm HeII}}{n_{\rm He}}\right] = \Gamma_{\rm HeI} n_e \frac{n_{\rm HeI}}{n_{\rm He}} + \beta_{\rm HeI} n_e \frac{n_{\rm HeI}}{n_{\rm He}} - \beta_{\rm HeII} n_e \frac{n_{\rm HeII}}{n_{\rm He}} - (\alpha_{\rm HeII} + \xi_{\rm HeII}) n_e \frac{n_{\rm HeII}}{n_{\rm He}} + \alpha_{\rm HeIII} n_e \frac{n_{\rm HeIII}}{n_{\rm He}}\,, \tag{2}$$

and

$$\frac{d}{dt}\left[\frac{n_{\rm HeIII}}{n_{\rm He}}\right] = \Gamma_{\rm HeII} n_e \frac{n_{\rm HeII}}{n_{\rm He}} + \beta_{\rm HeII} n_e \frac{n_{\rm HeII}}{n_{\rm He}} - \alpha_{\rm HeIII} n_e \frac{n_{\rm HeIII}}{n_{\rm He}}\,, \tag{3}$$

where $n_{\rm HeI}$, $n_{\rm HeII}$ and $n_{\rm HeIII}$ are respectively the number densities of the neutral, the singly-ionized and the doubly-ionized helium and $n_{\rm He} \equiv n_{\rm HeI} + n_{\rm HeII} + n_{\rm HeIII}$ is the total number density of helium. Assuming ionization equilibrium, the electron number density is given by

$$n_e = n_{\rm HII} + n_{\rm HeII} + 2n_{\rm HeIII}\,. \tag{4}$$

The functions used in the ionization equations are the photo-ionization rate $\Gamma_{\rm X}$, the recombination rate $\alpha_{\rm X}$, the dielectronic recombination rate $\xi_{\rm X}$, and the collisional ionization rate $\beta_{\rm X}$. The label X stands for the species used in this calculation, X $\in$ {H I, H II, He I, He II, He III}. We adopt the value of each photo-ionization state $\Gamma_{\rm X}$ from HM12, which takes into account the photo-ionization heating of H I, He I and He II , and Compton heating. The other functions adopted in our calculation, $\alpha_{\rm X}$, $\beta_{\rm X}$ and $\xi_{\rm X}$, and are summarized in Appendix A1 (Spitzer 1978; Verner & Ferland 1996). These values depend on the gas temperature and one has to compute the evolution of the gas temperature simultaneously together with the set of above four equations for the above mentioned ionization states.

2.2 Gas temperature

While the evolution of each ionization state depends on the temperature of gas in the IGM, the gas temperature also depends on the value of the local density and the flux of the background radiation through the heating or cooling processes. Assuming that the IGM is in the thermal equilibrium, which means the electrons, ions and neutrals have a common temperature, the gas temperature can be characterized by the electron temperature and the entropy equation can be written as (Mo et al. 2010):

$$\frac{d\ln T_{\rm g}}{d\ln(1+z)} = (\gamma - 1)\left[3 + \frac{1}{(\gamma-1)}\frac{d\ln\mu}{d\ln(1+z)} - \frac{\mathcal{H}-\Lambda}{H(z)\,n\,k_{\rm B}T_{\rm g}}\right]\,, \tag{5}$$

where n is the baryon number density, γ is the adiabatic index, μ is the mean molecular weight, and $H(z)$ is the Hubble parameter. $\mathcal{H}$ and Λ are the heating and cooling functions, respectively. We adopt the HM12 heating function $\mathcal{H}$, wheres the cooling function used in this work is summarized in Appendix A2 (Black 1981; Cen 1992). The first term in the right hand side of Eq. (5) corresponds to the adiabatic cooling through the Hubble expansion.

To describe the local density contrast of baryons, we define the local number density of each baryon component as,

$$n_{\rm X} \equiv (1+\delta)\, f_{\rm b}\, \bar{n}_{\rm X} = \Delta_{\rm b}\, \bar{n}_{\rm X}\,, \tag{6}$$

where δ is the matter density fluctuations, $f_{\rm b}$ represents the bias, $\bar{n}_{\rm X}$ is the average number density of a component X, and

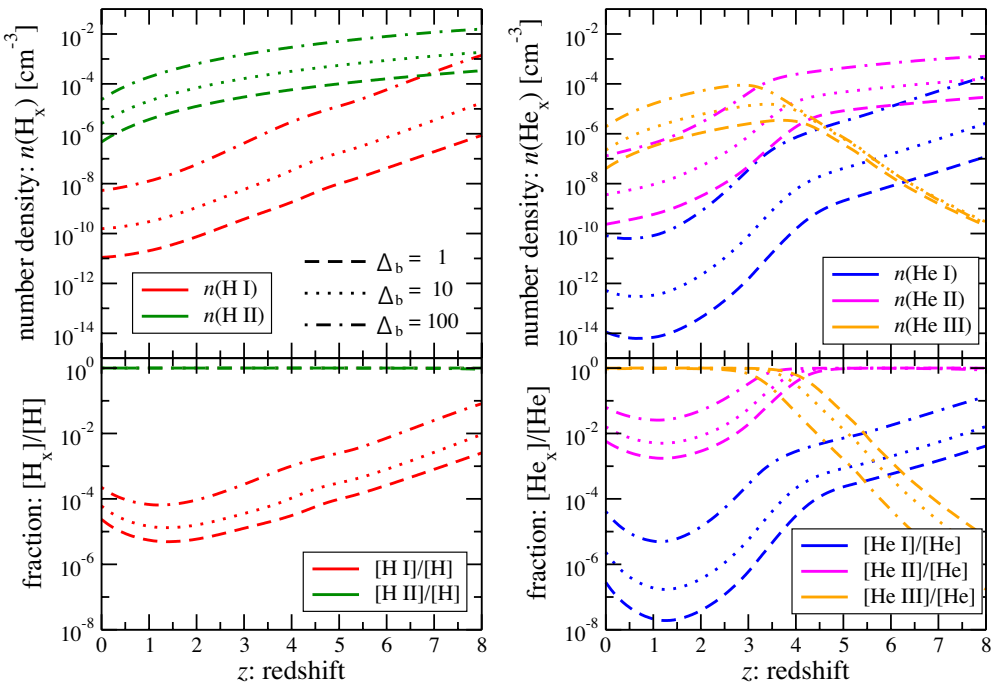

Figure 1. The redshift evolution of the ionization state of hydrogen (Left) and helium (Right). The top panels show the number density of each ionization state, while the bottom panels show their fractional abundance against the total number of hydrogen $n_{\mathrm{H_x}}/n_{\mathrm{H}}$ or helium $n_{\mathrm{He_x}}/n_{\mathrm{He}}$; the label X stands for each atomic ionization state. The lines corresponding to each species are as follows: H I (red), H II (green) He I (blue), He II (magenta) and He III (orange). The different line types represent the different values of the baryon density contrast parameter Δ_{b} defined in Eq. (6), and dashed, dotted and dashed-dot lines, respectively, correspond to Δ_{b} =1, 10 and 100.

the baryon density contrast is Δ_{b} (defined as $(1+\delta)\, f_{\mathrm{b}}$). Although the distribution of baryons might be different from that of matter, this effect is assumed to be small on the scales of interest in this work i.e. $f_{\mathrm{b}} = 1$.

The interaction time scales of the ionization and recombination for each species are given by $t_{\mathrm{X}}^{\mathrm{ion}} = (\Gamma_{\mathrm{X}} + \beta_{\mathrm{X}} n_e)^{-1}$ and $t_{\mathrm{X}}^{\mathrm{rec}} = (\alpha_{\mathrm{X}} n_e)^{-1}$, respectively. If these time scales are much shorter than Hubble time, the assumption of the ionization equilibrium is valid. For example, the typical time scales for hydrogen in the IGM are $t_{\mathrm{HI}}^{\mathrm{ion}} \sim (10^{-14}/\Gamma_{\mathrm{HI}}) \times 10^7$ years and $t_{\mathrm{HII}}^{\mathrm{rec}} \sim \Delta_{\mathrm{b}}^{-1} \times 10^{11}$ years at $z = 0$ for ionization and recombination, respectively. Since the recombination time scale is longer than the Hubble expansion time within low-density regions, the assumption of the ionization equilibrium is not satisfied for hydrogen. However, if the photoionization rate is much larger than the recombination rate, the timescale is actually quite short compared to the Hubble time and the assumption of equilibrium is reasonably satisfied. Furthermore, the assumption of ionization equilibrium is valid for high-densities ($\Delta_{\mathrm{b}} \gtrsim 10$), such as in filamentary structures in the IGM. In such a region, the local thermal equilibrium is also reasonably satisfied, since the interactions between the electrons and ionized species work effectively.

Assuming equilibrium, we solve these five independent equations Eqs. (1)-(5) simultaneously. The results of the abundance for the baryon density parameter, $\Delta_{\mathrm{b}} = 1$, 10 and 100 are shown in Figure 1. Note that the assumption of the equilibrium is invalid for $\Delta_{\mathrm{b}} = 1$, but we still show it for comparison purposes.

2.3 Spin temperature

In this subsection, we discuss the evaluation of the spin temperature and its coupling factors due to collisions and to the Wouthuysen-Field effect for both neutral hydrogen H I and singly-ionized isotope helium-3 ^{3}He II.

The relative abundance of the hyperfine excited state and the ground state is determined by the spin temperature T_{s} as

$$\frac{n_1}{n_0} = (g_1/g_0) \exp\left[-\frac{h_{\mathrm{p}}\nu_{10}}{k_{\mathrm{B}} T_{\mathrm{s}}}\right], \tag{7}$$

where n_1 and n_0 are the numbers of hyperfine excited state and the ground state, respectively. The factor g_1/g_0 is the

Species	λ_{10} [cm]	ν_{10} [MHz]	A_{10} [s^{-1}]	λ_α [Å]	f_α	g_1/g_0	primordial abundance
H I	21.1	1420.4	2.876×10^{-15}	1215.67	0.4162	3/1	—
^{3}He II	3.46	8665.7	1.959×10^{-12}	303.78	0.4162	1/3	1.0×10^{-5}

Table 1. The parameters related to the hyperfine transitions for H I and ^{3}He II. λ_{10} and ν_{10} are the wave-length and frequency corresponding to the energy of the hyperfine transition, A_{10} is the spontaneous decay rate†, λ_α and f_α are the wavelength and the oscillator length of the Lyα transition, respectively, and g_1/g_0 is the statistical weight of first-excited/ground state. The primordial abundance for ^{3}He is expressed as the fractional abundance against hydrogen, i.e. ^{3}He/H.

statistical weight of first-excited/ground state, $h_{\rm p}$ is the Planck constant, $k_{\rm B}$ is the Boltzmann constant, ν_{10} is the frequency which corresponds to the energy of the hyperfine transition.

The spin temperature is determined by three processes. The first is coupling to the CMB temperature which, due to to the Rayleigh-Jeans tail, can excite the hyperfine line. The second is the collisional excitation or de-excitation of the spin states. The third is the change of the spin states through the absorption and spontaneous re-emission of a Lyα photon or any Lyman-series photon (Madau et al. 1997; Shaver et al. 1999; Hirata 2006; Furlanetto & Pritchard 2006; Pritchard & Furlanetto 2006). The first process couples the spin temperature to the CMB photons, whereas the other two processes couple it to the gas. As a result the spin temperature is (Field 1958)

$$T_{\rm s} = \frac{(T_{\rm CMB} + y_{\rm c}T_{\rm k} + y_\alpha T_\alpha)}{(1 + y_{\rm c} + y_\alpha)}\,, \tag{8}$$

where $T_{\rm CMB}$ is the CMB temperature, $T_{\rm k}$ is the kinetic temperate of gas, T_α is the brightness temperature of the Lyα radiation field, $y_{\rm c}$ and y_α are the coupling factors of the collisional process and the Wouthuysen-Field process. The coupling factors can be written as

$$y_{\rm c} = \frac{C_{10}}{A_{10}}\frac{T_*}{T_{\rm k}}\,, \qquad y_\alpha = \frac{P_{10}}{A_{10}}\frac{T_*}{T_\alpha}\,, \tag{9}$$

where A_{10} is the spontaneous decay rate from state 1 to 0, C_{10} is the rate of collisional de-excitation, P_{10} is the rate of de-excitation due to the absorption of a Lyα photon, and T_* is the equivalent temperature defined as $T_* \equiv h_{\rm p}\nu_{10}/k_{\rm B}$.

In general, the rate of collisional de-excitation is written as

$$C_{10} = n_e\sqrt{\frac{k_{\rm B}T_{\rm k}}{\pi m_e c^2}}c\bar{\sigma}\,, \tag{10}$$

and $\bar{\sigma}$ is the averaged cross-section for spin exchange, given by

$$\bar{\sigma} = \frac{1}{(k_{\rm B}T_{\rm k})^2}\int_0^\infty dE\sigma(E)Ee^{-E/(k_{\rm B}T_{\rm k})}\,, \tag{11}$$

where $\sigma(E)$ is the cross-section for spin exchange as a function of collision energy.

The rate of de-excitation due to the absorption of Lyα photons is

$$P_{10} = \frac{4\pi e^2 f_\alpha}{m_e c}\begin{cases} \dfrac{4}{27}J_\alpha & \text{for H I} \\ \dfrac{4}{9}J_\alpha & \text{for } ^3\text{He II} \end{cases} \tag{12}$$

where e is the electron charge, m_e is the electron mass, f_α is the oscillator length of the Lyα transition, J_α is the flux at Lyα wave-length, and g_1/g_0 is the statistical weight of the first-excited/ground state. These values are defined for each hyperfine structure and we summarize some values related to these processes in Table 1. We give the detailed values on these rates for H I and ^{3}He II in the following sections.

2.3.1 H I : neutral hydrogen

For collisional excitations of neutral hydrogen (H I), the main process is the collision with electrons, while collisions with protons or other neutral hydrogen atoms are sub-dominant. The total rate of collisional de-excitation can be expressed as the summation of these three processes;

$$C_{10}^{\rm H\,I} = \left[\kappa_{10}^{\rm HH}(T_{\rm k})n_{\rm H} + \kappa_{10}^{e{\rm H}}(T_{\rm k})n_e + \kappa_{10}^{p{\rm H}}(T_{\rm k})n_p\right]\,, \tag{13}$$

where $\kappa_{10}^{\rm HH}$, $\kappa_{10}^{e{\rm H}}$ and $\kappa_{10}^{p{\rm H}}$ are the collisional rates of H-H, e-H and p-H processes, respectively. One can can find the collisional rates as functions of the kinetic temperature $T_{\rm k}$ in Zygelman (2005); Sigurdson & Furlanetto (2006); Furlanetto & Furlanetto (007a); Furlanetto & Furlanetto (007b).

† The values of A_{10} for some of the materials which is interesting on radio astronomy can be found in (Townes 1957; Gould 1994; Sunyaev 1966; Goldwire & Goss 1967).

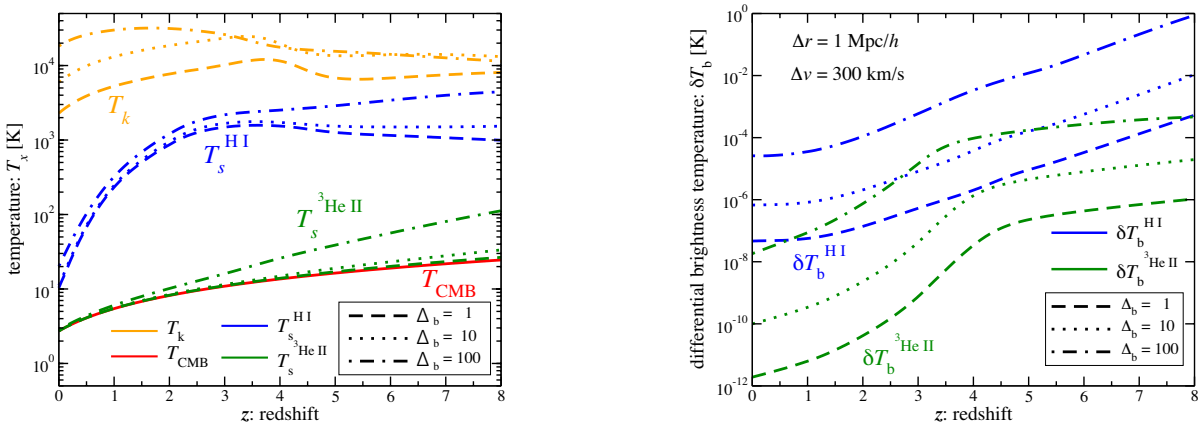

Figure 2. (Left) The redshift evolution of the , (from top to bottom) kinetic temperature $T_{\rm k}$ (orange), the spin temperature of H I (blue) and ^{3}He II (green), and the CMB temperature $T_{\rm CMB}$ (red). (Right) The evolution of the differential brightness temperature of H I and ^{3}He II as functions of redshift. In both panels, the different line types represent the different values of the baryon density contrast parameter $\Delta_{\rm b}$, and the dashed, dotted and dot-dashed lines, respectively, correspond to $\Delta_{\rm b} = 1$, 10 and 100. For the estimation of the differential brightness temperature, we assume a simple slab model in which the filament is 1 Mpc/h wide ($\Delta r = 1$ Mpc/h) and the proper line-of-sight velocity is $\Delta v = 300$ km/s.

For the Wouthuysen-Field process of H I, following Eq. (12), the de-excitation rate is related to the radiation field as

$$P_{10}^{\rm HI} = \frac{16\pi e^2 f_\alpha^{\rm HI}}{27 m_e c} J_{{\rm Ly}\alpha,{\rm HI}}\,, \tag{14}$$

where $f_\alpha^{\rm HI} = 0.4162$ is the oscillator length of the H I Lyα transition, and $J_{{\rm Ly}\alpha,{\rm HI}}$ is the flux at H I Lyα wave-length ($\lambda_{{\rm Ly}\alpha,{\rm HI}} = 1216$Å).

2.3.2 ^{3}He II : singly-ionized isotope helium-3

The most dominant process of collisional coupling for the singly-ionized isotope helium-3 (^{3}He II) is collisions with electrons. Then, following Eq. (13), the collisional rate can be written as

$$C_{10}^{^3{\rm HeII}} = n_e \sqrt{\frac{k_{\rm B} T_{\rm k}}{\pi m_e c^2}}\, c\, \bar{\sigma}^{e\,^3{\rm He}}\,, \tag{15}$$

where $\bar{\sigma}^{e\,^3{\rm He}}$ is the average cross-section of spin exchange between ^{3}He II and electrons, which can be approximated as (McQuinn & Switzer 2009),

$$\bar{\sigma}^{e\,^3{\rm He}} \simeq \frac{14.3{\rm eV}}{k_{\rm B} T_{\rm k}} a_o^2\,, \tag{16}$$

where a_o is the Bohr radius.

For the Wouthuysen-Field process of ^{3}He II, the de-excitation rate can be estimated from Eq. (12) in the same manner as the case of H I and given by

$$P_{10}^{^3{\rm HeII}} = \frac{16\pi e^2 f_\alpha^{\rm HeII}}{9 m_e c} J_{{\rm Ly}\alpha,{\rm HeII}}\,, \tag{17}$$

where $f_\alpha^{\rm HeII} = 0.4162$ is the oscillator length of the He II Lyα transition, and $J_{{\rm HeII},{\rm Ly}\alpha}$ is the flux at He II Lyα wavelength ($\lambda_{{\rm Ly}\alpha,{\rm HeII}} = 304S$Å). In both cases, i.e. for H I and ^{3}He II, one has to assume a model for the Ly-α flux as a function of redshift. Throughout this paper, the recent model of UV/X-ray background from HM12 is used.

The spin temperature is computed with the assumption that the kinetic temperature $T_{\rm k}$ and the color temperature T_α are coupled to the gas temperature $T_{\rm g}$; i.e. $T_{\rm k} \simeq T_\alpha \simeq T_{\rm g}$. The evolution of the spin temperature of H I and ^{3}He II are shown in the left panel of Figure 2, and the kinetic temperature ($T_{\rm k}$) and the temperature of CMB ($T_{\rm CMB}$) are also plotted in the same panel.

Although the contribution of the radiative coupling to the spin temperature is weak at low-redshifts, it becomes important around the EoR. Moreover some exotic models show that the contribution of X-ray alters the history of reionization dramatically (Furlanetto et al. 2006; Shchekinov & Vasiliev 2007), and uncertainties sill remain on the estimation of the spin temperature around the EoR and at even higher-redshift.

2.4 Differential brightness temperature

In radio astronomy, the measured radiation is expressed in terms of the differential brightness temperature, namely, the difference between the brightness temperature of the object to that of the CMB; which is given by

$$\delta T_{\rm b}^{\rm X}(z) \equiv T_{\rm b}^{\rm X}(z) - T_{\rm CMB}(z) = \frac{[T_{\rm s}^{\rm X}(z) - T_{\rm CMB}(z)](1 - e^{-\tau_{\rm X}(z)})}{1+z}\,, \tag{18}$$

where $T_{\rm b}^{X}$ is the brightness temperature and $\tau_{\rm X}(z)$ is the optical depth, where X marks either H I or ^{3}He II. In general, the optical depth is (Furlanetto et al. 2006)

$$\tau_{\rm X}(z) = \frac{g_1}{g_0+g_1}\frac{c^2 h_{\rm p} A_{10}}{8\pi\nu_{10}^2 k_{\rm B}}\frac{n_{\rm X}(z)}{T_{\rm s}^{\rm X}(z)}\frac{1}{(dv_\parallel/dr_\parallel)}\,, \tag{19}$$

where $n_{\rm X}(z)$ is the number density of species X, and $dv_\parallel/dr_\parallel$ is the velocity gradient along the line-of-sight, including both the Hubble expansion and the peculiar velocity (Kaiser 1987).

In the optically thin regime (i.e. $\tau \ll 1$), Eq. (18) can be rewritten as

$$\begin{aligned}\delta T_{\rm b}^{\rm X}(z) &\simeq \frac{\left[T_{\rm s}^{\rm X}(z) - T_{\rm CMB}(z)\right]\tau_{\rm X}(z)}{1+z} \\ &\simeq \frac{g_1}{g_0+g_1}\frac{c^2 h_{\rm p} A_{10}}{8\pi\nu_{10}^2 k_{\rm B}}\frac{n_{\rm X}(z)\Delta r}{(1+z)\Delta v}\left(1 - \frac{T_{\rm CMB}(z)}{T_{\rm s}^{\rm X}(z)}\right)\,,\end{aligned} \tag{20}$$

where Δr denotes the line-of-sight width of the filamentary structure and Δv denotes the proper line-of-sight velocity. Eq. (20) shows that the differential brightness temperature can be observed in emission(absorption) signal when the spin temperature is larger(smaller) than the CMB. In the second line in Eq. (20), we used the optical depth given by Eq. (19).

2.5 Signal estimation for a simple slab model

In order to calculate the signal we first assume a simple elongated slab model with constant density. The filament slab is assumed to have a width $\Delta r = 1$ Mpc$/h$ and the proper line-of-sight velocity $\Delta v = 300$ km/s. The H I column density of this filament corresponds to $N_{\rm HI} = n_{\rm HI}\Delta r \simeq 10^{15} - 10^{16}$ cm^{-2} with $\Delta_{\rm b} = 100$ around the present redshift. We show the differential brightness temperature of H I and ^{3}He II in the right panel of Figure 2 for the different values of the baryon density contrast parameter, $\Delta_{\rm b} = 1$, 10 and 100.

The emission from ^{3}He II shows a different redshift dependence rerative to that of H I. This is because the reionization state of H I is different from that of He. The drop in $\delta T_{\rm b}^{^3{\rm HeII}}$ around $z \sim 4$ corresponds to the epoch of He II reionization (He II$\rightarrow$He III), where the fraction of He II for the total helium components decreases after that. Therefore, it is expected that it becomes more difficult to observe ^{3}He II emission after $z \sim 4$. However the advantage of the observation with high-frequencies at low-redshifts also motivates us to attempt to probe the baryons in the filamentary structures through the emission line of the hyperfine transition of ^{3}He II.

3 SIGNAL ESTIMATION FROM N-BODY SIMULATIONS

In the previous section, we calculated the brightness temperature of the hyperfine emission assuming the overdensity δ, the proper line-of-sight velocity Δv and the width Δr of the filament. As a next step, we carry out the same calculation but with filaments taken from a cosmological N-body for the large-scale structure. In this section the N-body simulations used to make the large-scale structures and the procedure to estimate the signal of hyperfine transition from them are described. Furthermore, a number of elongated filamentary structure and their observed signal as seen from various viewing angles are considered.

3.1 N-body Simulation

To obtain the N-body 512^3 particles simulation a parallel Tree-Particle Mesh code *Gadget*-2 (Springel 2005) in its full Tree-PM mode was run. The simulation size is 120 Mpc$/h$ on a side, the minimum mass resolution corresponds to $9.68\times10^8 M_\odot/h$ and, as mentioned before, adopts the WMAP-7yrs cosmological model. The matter density field estimated through the N-body simulation at the present time is shown in Figure 3. The frames and the symbols represent the appropriately-determined filamentary structures and their center positions.

We here estimate the signal of the hyperfine transition for H I and ^{3}He II based on the N-body simulation of the large-scale structures. To calculate the brightness temperature, we first divide the simulation box into 256^3 grids and estimate the density contrast $\delta \equiv (\rho - \bar\rho)/\bar\rho$ and the proper line-of-sight velocity Δv with Cloud-in-Cell (CIC) interpolation on each grid. Then the differential brightness temperature is calculated through Eq. (18) adopting the values of the density contrast and

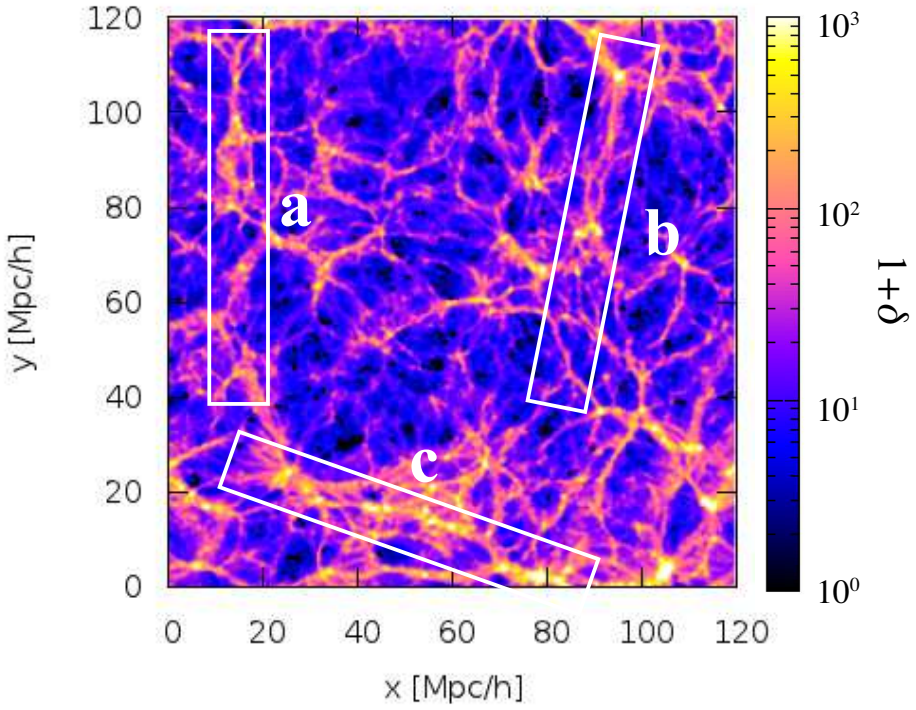

Figure 3. This figure show a slice of depth 1.4 Mpc/h of the density field through the N-body simulation at the present redshift. The color-bar represents the over density $1+\delta$. The boxes and symbols are the appropriately-defined filamentary structures and their center positions.

the proper line-of-sight velocity on each grid. Both signals from H I and ^{3}He II are evaluated according to the description in Sec. 2.

Figures 4 and 5 show the differential brightness temperature of thin slices across the simulation box at different redshifts for H I and ^{3}He II respectively. The simulation outputs are shown at $z = 0$, 1, 2 and 4. The depth of each slice is 1.4 Mpc/h in all cases, where the two-dimensional maps shown in the figures are integrated over the depth. The depth of 1.4 Mpc/h corresponds to the frequency bandwidth of ∼0.7 MHz for the H I survey and ∼ 4 MHz for the ^{3}He II survey at $z = 0$.

The filamentary structures in both cases is seen through the brightness temperature, where the amplitudes are $\delta T_{\rm b} \sim 10^{-6}$ K for H I and $\sim 10^{-9}$ K for ^{3}He II in the maps at $z = 0$. The signals are lower than the case we calculated earlier, assuming a slab filamentary structure with constant baryon overdensity $\Delta_{\rm b} \simeq 100$ (see the right panel of Figure 2) – this also applies for higher redshifts. One can clearly see from Figure 3 that at present time the density contrast of the filaments is $\Delta_{\rm b} \lesssim 100$, which explains the lower values we obtain. We can also clearly see the drastic change in the intensity of ^{3}He II from $z = 4$ to $z = 2$, which reflects the He II reionization.

3.2 Signal from a filamentary structure

Filaments can extend to very large distances reaching many tens of mega-parsecs, as seen in simulations and in real observations (Erdoğdu et al. 2004; Choi et al. 2010; Pandey et al. 2011). When a filament is elongated along the line-of-sight direction one expects to detect the highest signal from the filamentary structure. Conversely, when the filament and the line-of-sight direction are perpendicular to each other, the signal should be lower than the former case. Therefore, the signal from a filamentary structure depends on the viewing angle relative to the line-of-sight direction.

The brightness temperature, $\delta T_{\rm b}$ of the three filaments is shown in Figure 3 and are labeled with "a", "b" and "c". We take the signal within a cylindrical region that passes along the line of sight, which we refer to as the observational skewer. The cross section of the skewer represents the telescopes beam, i.e., resolution. The skewer is assumed to be on the x-y plane for each filament shown in Figure 3 and rotate a skewer by an angle θ around the center of the filament. The thickness of the skewer corresponds to the spatial resolution with which one observes. The positional relation between the filamentary structures and the observed skewer is shown in Figure 6. The cartoon is shown on the plane that is define by the filament and the line-of-sight directions. Here θ represents the angle between the filament and the obvervational skewer. The $\theta = 0^\circ$ is defined such that the line-of-sight direction is parallel to the filament long axis. The signal at zero redshift as a function of

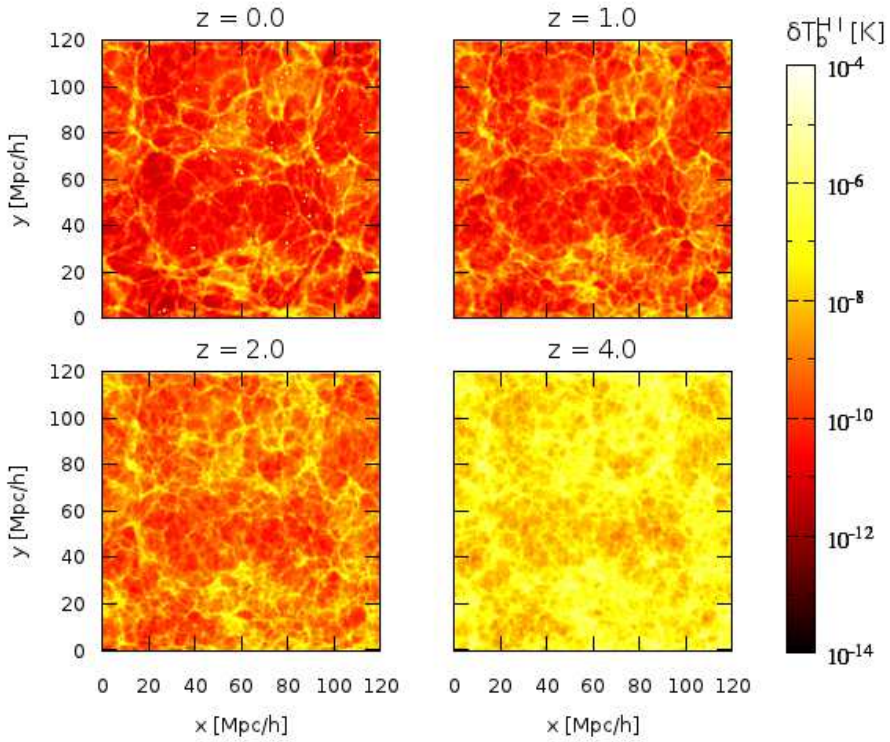

Figure 4. Maps of the differential brightness temperature of H I at at $z = 0$ (Top-Left), $z = 1$ (Top-Right), $z = 2$ (Bottom-Left) and $z = 4$ (Bottom-Right). We take the density contrast and the proper line-of-sight velocity from the snapshots of the N-body simulation and then calculate the differential brightness temperature through Eq. (18). All slices are 120 Mpc/h on the side and the depth of 1.4 Mpc/h.

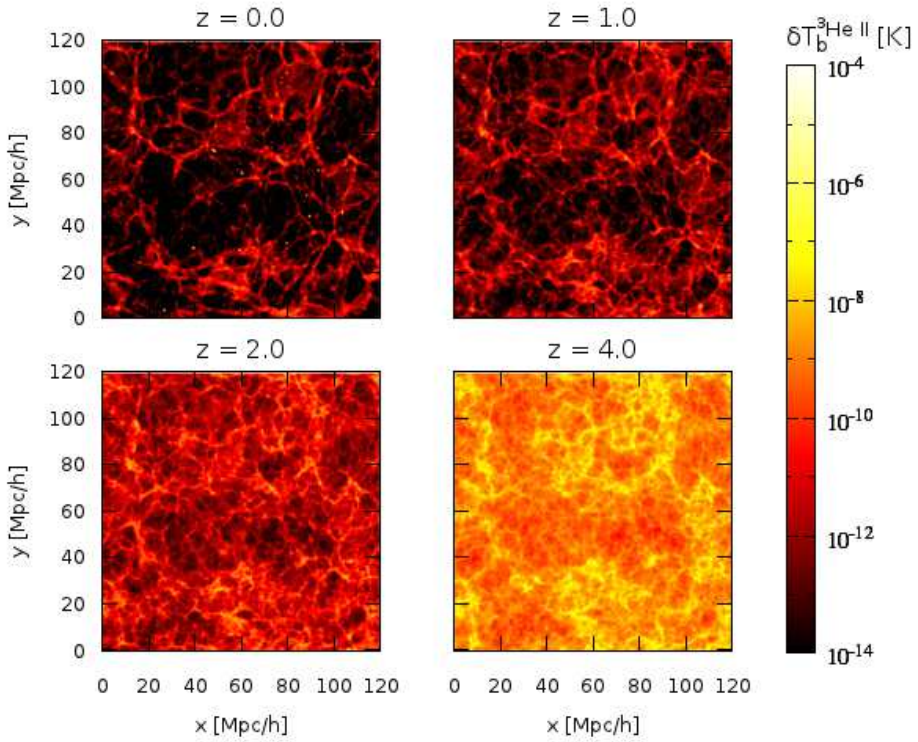

Figure 5. Same as Figure 4, except the maps are for the differential brightness temperature of ^{3}He II.

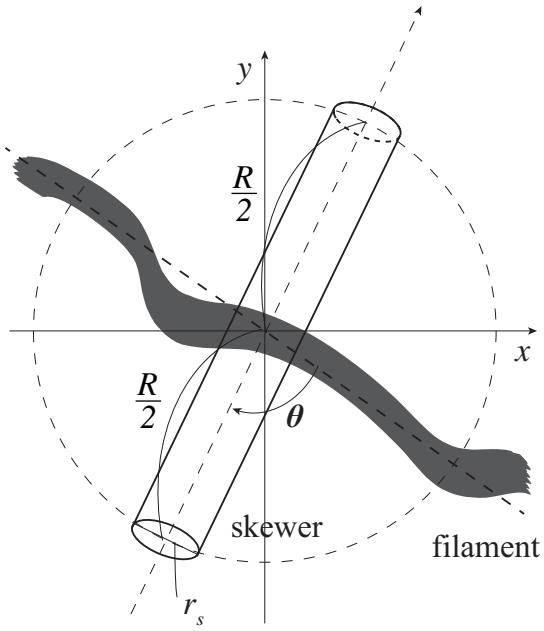

Figure 6. The positional relation between the filamentary structures and the observational skewer. Here, θ represents the angle between the skewer and long axes of the filament's. R and r_s represent the length along the line-of-sight and the spacial resolution of the skewer. The line-of-sight and of the filament's long axes direction define the x-y plane.

the viewing angle for H I is shown in Figure 7 and for ^{3}He II in Figure 8. In these figures, the results for the different values of the spacial resolution, $r_s = 1$, 3, 5 and 10 Mpc/h is shown, and the length of the skewer is $R = 100$ Mpc/h for all cases.

We should note that these results have no contribution from the high-density region whose density contrast is $\delta \geqslant 200$ because we masked the signal from such regions to eliminate the contributions from galaxies. On the other hand, the haloes with small mass which is often called as minihalo may also contributes to signal along the line of sight, but our simulation does not have enough resolution to resolve such haloes.

The small spikes seen in Figures 7 and 8 reflect the contributions from the other structures around the filament. Compared to filaments a and b, filament-c has more widespread structure which explains the weak angular dependence of filament-c. It is clear that if one observes a filament, which extends along the line-of-sight, the amplitude of the expected emission signal is stronger. For example, in the case of filament-a, $\delta T_{\rm b} \sim 10^{-5}$ K for H I and $\sim 10^{-8}$ K for ^{3}He II assuming spatial resolution of $r_s = 1$ Mpc/h, which are more than 10 times larger than the case in which the two directions are perpendicular. Furthermore, for coarser resolution (thicker skewer), the signal is also expected to be higher. In the following sections, the prospects for observing the signals of the hyperfine transition are discussed.

4 PROSPECT OF OBSERVATION

4.1 Observational sensitivity

In this subsection, we summarize the sensitivity of relevant radio-telescope to estimate the prospects for observing the signals of H I and ^{3}He II. Here we consider single dish and interferometric radio telescopes, and for each case we estimate the noise level expected, using the expressions of Furlanetto et al. (2006).

The resolution of the radio-telescope can not exceed the diffraction limit, which depends on the largest dimension of the telescope $D_{\rm max}$ and the observing frequency λ as $\theta_{\rm D} = \lambda/D_{\rm max}$.

The sensitivity or the brightness temperature uncertainty of radio telescope is

$$\delta T_{\rm N}(\lambda) \simeq \frac{\lambda^2/\theta_{\rm s}^2}{A_{\rm tot}} \frac{T_{\rm sys}}{\sqrt{\Delta\nu t_{\rm obs}}}\,, \tag{21}$$

where λ is the observing frequency, $\theta_{\rm s}$ is the angular resolution, $T_{\rm sys}$ is the system temperature, $A_{\rm tot}$ is the total collecting area, $\Delta\nu$ is the band width, and $t_{\rm obs}$ is the integration time of the observation.

The system temperature is given by

$$T_{\rm sys} \equiv T_{\rm sky} + T_{\rm rec}, \tag{22}$$

Telescope	$R_{\rm dish}$ [m]	$N_{\rm dish}$	$A_{\rm tot}$ [m^2]	$\epsilon_{\rm ap}$	Operating range	$D_{\rm max}$ [km]
Single dish						
GBT	100	—	7,850	0.7	100 MHz - 116 GHz	0.1
Arecibo	305	—	73,000	0.8	47 MHz - 10 GHz	0.3
FAST	500	—	200,000	0.8	70 MHz - 3 GHz	0.5
Interferometers						
EVLA	25	27	13,300	0.8	1,000 MHz - 50 GHz	1 - 36
GMRT	45	30	60,750	0.8	50 MHz - 1.5 GHz	25
MeerKAT (phase 2)	13.5	64	9,160	0.8	580 MHz - 14.5 GHz	20
SKA (phase 2)	15	1,500	300,000	0.8	70 MHz - 10 GHz	5c

Table 2. The characteristic parameters for the specification of the radio-telescopes. GBT and Arecibo are the single dish telescopes and the others are the radio-interferometers. $R_{\rm dish}$ is the diameter of a dish for one telescope, $N_{\rm dish}$ is the number of telescopes, and $A_{\rm tot}$ is the effective total collecting area of the telescope. The parameter $\epsilon_{\rm ap}$ represents the aperture efficiency of a dish. $D_{\rm max}$ is the maximum base line length of the telescope; for EVLA the value depends on the configuration of the telescopes, and for SKA we take the extent of compact core.

where the first term is due to the sky itself and is dominant at low frequencies ($\nu \lesssim 150$MHz), whereas the second is due to the receiver and dominates at high frequencies ($\nu \gtrsim 150$MHz).

The sky temperature at high-latitude is roughly given as

$$T_{\rm sky} \sim 180\,(\nu/180{\rm MHz})^{-2.6}\,{\rm K}\,. \tag{23}$$

Therefore, the noise of the interferometer due to the sky can be written using Eq. (21) as,

$$\delta T_{\rm N}^{\rm sky}(\nu) \simeq 5.0\,\epsilon_{\rm ap}^{-1}\left(\frac{10^5\ {\rm m}^2}{A_{\rm tot}}\right)\left(\frac{1'}{\Delta\theta}\right)^2\left(\frac{1+z}{1}\right)^{4.6}\left(\frac{1420\,{\rm MHz}}{\nu_0}\right)^{4.6}\left(\frac{\rm MHz}{\Delta\nu}\frac{100\ {\rm hr}}{t_{\rm obs}}\right)^{1/2}\ \mu{\rm K}\,, \tag{24}$$

where $\epsilon_{\rm ap}$ is the aperture efficiency of a dish, ν is the observational frequency, $\Delta\theta$ is the beam angular resolution, and ν_0 represents the rest frame frequency of the observed hyperfine transition; i.e., ν_0=1420 MHz for H I or ν_0=8667 MHz for ^{3}He II.

Similarly, the noise due to the receiver, which is roughly frequency independent, can be written from Eq. (21);

$$\delta T_{\rm N}^{\rm rec} \simeq 23.9\,\epsilon_{\rm ap}^{-1}\left(\frac{T_{\rm rec}}{30\ {\rm K}}\right)\left(\frac{10^5\ {\rm m}^2}{A_{\rm tot}}\right)\left(\frac{1'}{\Delta\theta}\right)^2\left(\frac{1+z}{1}\right)^{2.0}\left(\frac{1420\,{\rm MHz}}{\nu_0}\right)^{2.0}\left(\frac{\rm MHz}{\Delta\nu}\frac{100\ {\rm hr}}{t_{\rm obs}}\right)^{1/2}\ \mu{\rm K}\,, \tag{25}$$

where $T_{\rm rec}$ is the receiver noise.

The total noise is given by combining Eqs. (24) and (25) as

$$\delta T_{\rm N} = \left(\delta T_{\rm N}^{\rm sky} + \delta T_{\rm N}^{\rm rec}\right) \times \begin{cases} 1 & \text{(single dish)} \\ 1/\sqrt{N_{\rm B}} & \text{(interferometer)}, \end{cases} \tag{26}$$

where $N_{\rm B} = N_{\rm dish}(N_{\rm dish}-1)/2$ is the number of pair-wise correlations or base lines, and $N_{\rm dish}$ is the number of interferometeric elements in the telescope. The noise for the interferometer can be reduced by a factor of $1/\sqrt{N_{\rm B}}$.

We consider the sensitivity of relevant current and future radio-telescopes: the Green Bank Telescope (GBT), the Arecibo Radio Telescope (Arecibo), the Five-hundred-meter Aperture Spherical Telescope (FAST), the Giant Metrewave Radio Telescope (GMRT), the Expanded VLA (EVLA), MeerKAT and the Square-Kilometer Array (SKA). The characteristic parameters for these radio telescopes are shown in Table 2. We should note that the operating range of GMRT does not have enough frequency range to observe the signal of ^{3}He II at low-redshifts and its achievable redshift range is $z > 4.7$. The operating range of FAST also does not reach the restframe frequency of ^{3}He II. However, future upgrade may allow to observe up to 8 GHz (Nan et al. 2011).

The H I and ^{3}He II differential brightness temperature and the sensitivities as a function of redshift for the slab model case are shown in Figures 9 and 10, respectively. The signal curves are the same as the ones shown in the right panel of Figure 2, whereas the solid curves in this figure show the sensitivity of the various telescopes. Figures 9 and 10 show three types of observation with different angular resolutions: $\Delta\theta$ =30, 10 and 1 arcmin. The system temperature includes the sky and receiver temperatures, where we assume that $T_{\rm rec} = 30$ K and $T_{\rm sky}$ is taken from Eq. (23). The sensitivity is given assuming 100 hours of integration time and a bandwidth $\Delta\nu = 30$ MHz for H I and $\Delta\nu$ =200 MHz for ^{3}He II. These values for the bandwidth correspond to ~ 100 Mpc/h depth along the line-of-sight around $z = 0.5$. We should note that, for our case, the sensitivity of EVLA and FAST are almost the same, hence, we only plot the sensitivity curve for FAST. The relationship between the comoving distance and the bandwidth is given in Appendix B.

As shown in Figures 4 and 5 for the case of the N-body simulations, the emission signal is expected to increase at higher redshifts for both H I and ^{3}He II. In Figures 11 and 12, we show the signal for the N-body simulations case again. The brightness temperature is shown for the three filamentary structures (a, b and c) at redshifts, $z = (0.1, 0.5, 1, 2, 4)$, for H I and ^{3}He II, respectively, assuming an angular resolution of 10 arcmin. We also plot the sensitivity curves for each survey in the same panels. The sensitivity is calculated in the same way as in Figures 7 and 8. The points show the brightness temperature

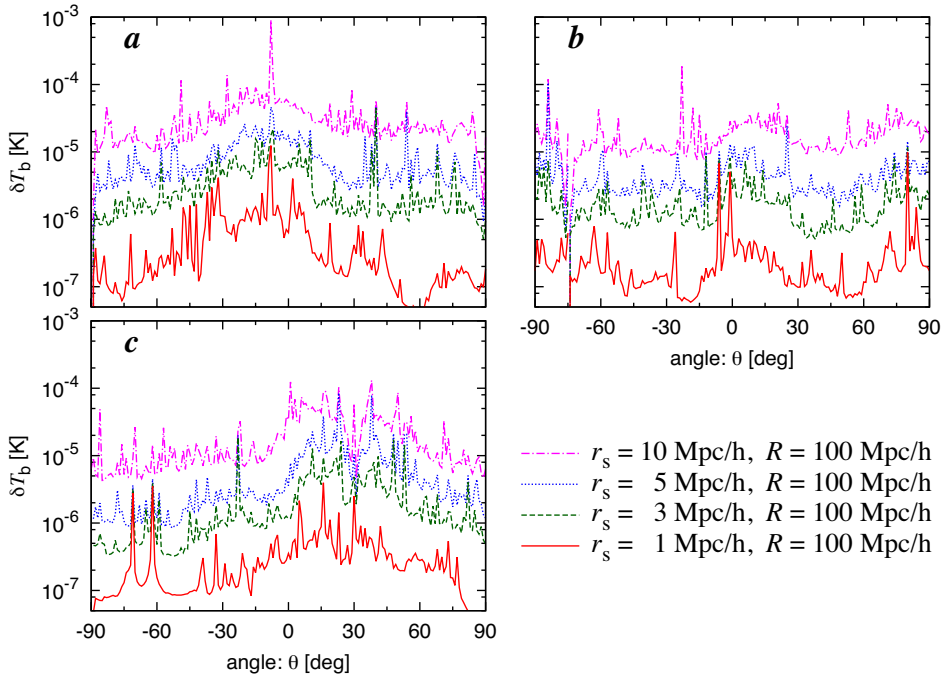

Figure 7. The signal of H I from the filamentary structures at $z = 0$. The angle θ represents the angular size between a filament and the line-of-sight, r_s and R represent the spacial size and the line-of-sight width for a skewer. The different color lines show the different values of r_s; which are 10 Mpc/h (magenta), 5 Mpc/h (blue), 3 Mpc/h (green) and 1 Mpc/h (red), and the width is fixed to be $R = 100$ Mpc/h for all cases. The positional relation between a filament and a skewer is pictured in Figure 6. The label "a", "b" and "c" correspond to the filaments shown in Figure 3.

for each filament at a given redshift averaged over the viewing angles. The bar represent and range of values of the observed temperature for the range of viewing angles, where the maximum is obtained at viewing angle of 0° and the minimum at viewing angle of 90°.

Figure 11 shows that for H I, the amplitude of signal is significantly larger than that of ^{3}He II. If we focus on the redshift range of $z \sim 0-1$, the brightness temperature is $\delta T_{\rm b} \sim 10^{-6}$ to 10^{-3} K with angular resolution of 10 arcmin, which corresponds to ~ 5.5 comoving Mpc/h at $z = 0.5$. The figure clearly shows that such filaments are in principle detectable with current radio telescopes up to high redshifts. The beam size of the present receiver for this frequency range is adequate; e.g., 9 arcmin for GBT and ~ 3.5 arcmin for Arecibo. We assume here 100 hours integration time. Note however that GMRT, EVLA and future telescopes may have enough sensitivity to detect the signal even with a shorter integration time.

On the other hand, compared to the signal of H I, the signal of ^{3}He II is much weaker and the amplitude is on the order of micro-kelvin at $z \sim 0-1$ as shown in Figure 12. The sensitivity is calculated assuming 10 arcmin resolution and 100 hours of observation time. Such a signal is very hard to detect by the currently available telescopes, maybe with the exception of GMRT. GMRT is the most suitable of the currently operational telescopes for the observation of ^{3}He II. Unfortunately, its operating frequency range is less than 1.5 GHz which is suitable for detecting ^{3}He II only at $z > 4.7$. Future telescopes however, will be able to detect such feeble emission after 100 hours of observation.

Obviously, the beam size at the frequencies relevant to ^{3}He II is smaller than that of the beam for H I due to the higher frequency of the transition. Therefore, the field of view for the observation is much smaller. In general, the field-of-view for the single dish telescope corresponds to the beam size, and the observing area are typically small. Due to the limited size of the beam relative to that of the objects of interest (filaments), the integrated sensitivity at high frequency is small, hence, a single dish telescope seems unsuitable for the detection of the ^{3}He II signal at low-redshifts. In comparison, the field-of-view of an interferometer is given by the dish size of a small telescope; $\theta_{\rm FoV} \simeq \lambda/R_{\rm dish}$. Therefore, interferometers typically have a larger field-of-view than the single dish telescopes, and one can obtain a larger skewer cross section, e.g. $\theta_{\rm FoV} \sim 4$ arcmin for EVLA and $\theta_{\rm FoV} \sim 8$ arcmin for MeerKAT. Future telescopes such as MeerKAT and SKA have enough sensitivity for detecting the ^{3}He II signal around these redshifts.

Furthermore, at higher redshift, $z \geqslant 2$, we still have possibility for detecting the ^{3}He II signal with present instruments such as Arecibo and EVLA. The angular size increases at higher redshifts, and the observing frequency decreases. The beam size of Arecibo reaches 3 arcmin at $z = 4$ and it corresponds to the spacial size of $r_s \sim 5$ Mpc/h. Around these redshifts,

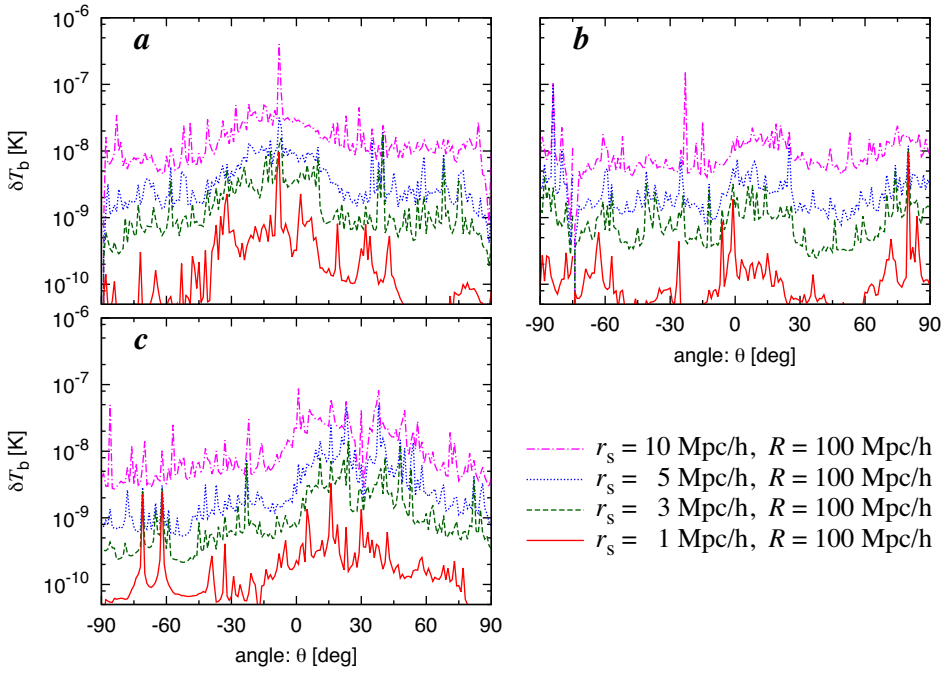

Figure 8. Same as Figure 7, but for the signals of ^{3}He II.

we can not use the galaxy catalogs of the optical galaxy redshift survey, but the results from the observation of Ly-α can be adopted as tracers to find the high-density regions.

4.2 Observational Issues

4.2.1 Observational Strategy:

The strategy for choosing the observing area and frequency is a key aspect for the detection of filaments with H I and He II. Obviously, for a highly sensitive instrument, like SKA, one can choose to survey large area and see whether there is any localized excess in the intensity of H I and He II which will imply large scale structure with excess neutral fraction of these specs.

The sensitivity of other instruments is not as good as SKA, therefore one has to adopt a different strategy for such a detection (this is also true for the initial and even intermediate stages of SKA. Therefore, for such instruments we assume some prior knowledge on the location of filaments. Namely, we use information from other observations would provide the necessary information on the location and orientation of filaments. Recent galaxy redshift surveys such as 2dF and SDSS have revealed the vast area of the universe at low-redshifts and determined the position of each galaxies. Such map of galaxies implies the existence of large filamentary structures and can provide the fruitful information to take aim at the location of filaments (Erdoğdu et al. 2004; Tempel et al. 2014). At higher redshifts one can resort in principle to Ly-α forest data.

4.2.2 Galactic Foregrounds:

Diffuse foregrounds at low frequencies are very prominent and might be orders of magnitude higher than the signal. For example, in the range of ≈ 150 MHz the foregrounds – which are dominated by diffuse synchrotron radiation and extra galactic point sources confusion – are about 3 orders of magnitude higher than the H I signal (Shaver et al. 1999; Jelić et al. 2008, 2010; Bernardi et al. 2009, 2010). However, even at such low frequencies the smooth spectral properties of the Galactic diffuse foregrounds and extra-galactic point sources allow their disentanglement from the cosmological signal of interest (Jelić et al. 2008; Harker et al. 2009; Chapman et al. 2012; Chapman et al. 2013). At higher frequencies the intensity of the foregrounds drops vey significantly; typically as $\propto \nu^{-2.6}$ (Shaver et al. 1999) which reduces the problem of foregrounds significantly around 1 GHz.

In addition to the different frequency dependent behavior of the signal from filaments with respect to the diffuse and point source foregrounds, their disentanglement requires a late bandwidth within which the two behaviors can be clearly seen. As an example we consider a $\Delta l \propto 100$ cMpc long filament elongated along the line of sight at $z \approx 1$. The signal from this filament

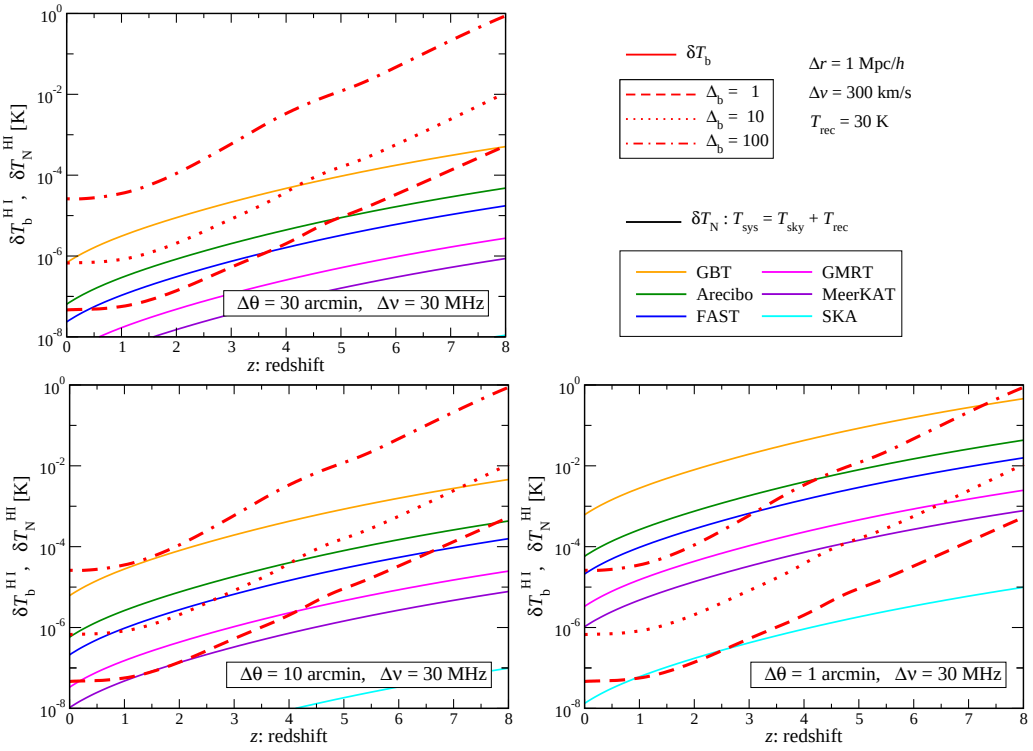

Figure 9. The signal and noise spectrum for the hyperfine transition of H I as a function of redshift. The signal represents the differential brightness temperature of H I (red-lines), which is same as shown in the right panel of Figure 2. The noise spectrum is adopted for the observation at the rest frame frequency of 1.4 GHz with GBT (orange), Arecibo (green), EVLA (violet), FAST (blue), MeerKAT(violet) and SKA (cyan), respectively. The solid curves represent the noise taking into account only the sky temperature, and the dashed curves with same color represent the noise taking into account both the sky temperature and the receiver noise of $T_{\rm rec} = 30$ K. The three panels show the difference of the noise spectra with the different values of the spacial resolution $\Delta\theta$ for the observation; we adopt the values to be $\Delta\theta = 30$ arcmin (Top-Left), $\Delta\theta = 10$ arcmin (Bottom-Left), and $\Delta\theta = 1$ arcmin (Bottom-Right), respectively. The frequency band width of $\Delta\nu = 30$ MHz, which corresponds to $\sim$100 Mpc/h width along the line-of-sight at $z = 0.5$, is adopted for all cases. We assume the 100 hours of integration time for all telescopes.

has has a frequency range of $\Delta\nu/\nu \approx \Delta v/c = H(z)\Delta l/c \approx 7\%$ which translates to less than 100 MHz. Such frequency range is much smaller than the observational bandwidth that current and future instrument have. Such an argument works over the whole range of redshifts that we have considered in this paper. Therefore, the foregrounds are a surmountable obstacle and will not pose a significant problem to the prospect of observing filaments with H I and He II.

4.2.3 Contamination from Virialized objects

Quantifying the contribution of H I and He II emission from galaxies or other virtualized is very difficult as there is very little data on H I beyond $z \approx 0$ and no data whatsoever on He II. Obreschkow et al. (2009) have simulated the expected source counts on the sky as a function of redshift where they estimated the number of radio sources above a certain flux limit as a function of redshift per squared degree within redshift bins of $\Delta z = 0.1$, $dN/dz/\mathrm{deg}^2$ (see Figure 5 in their paper). Using this figure, the number of sources above 1 μJy increases as $z^{2.3}$ at low redshifts; peaks at $z = 0.5$ and then drops exponentially at at higher redshifts. The peak value reaches a few time 10^5 sources which for a beam of a few arc minutes drops down to 10^3 at most. This is of course something that one should worry about, however, given that these source are very highly localized in frequency (Obreschkow et al. (2009) adopted a value of 8 km/sec width) it is straightforward to show that with a high frequency resolution data one can filter these objects by applying a low pass filter along the frequency direction. We plan to address this point in more detail in future work.

5 CONCLUSIONS

Observing the hyperfine transition of the intergalactic H I and ^{3}He II provides a useful probe for baryons in the high density regions of the diffuse IGM. These probes can help shed light on many problems, such as, the missing baryons and the large-scale

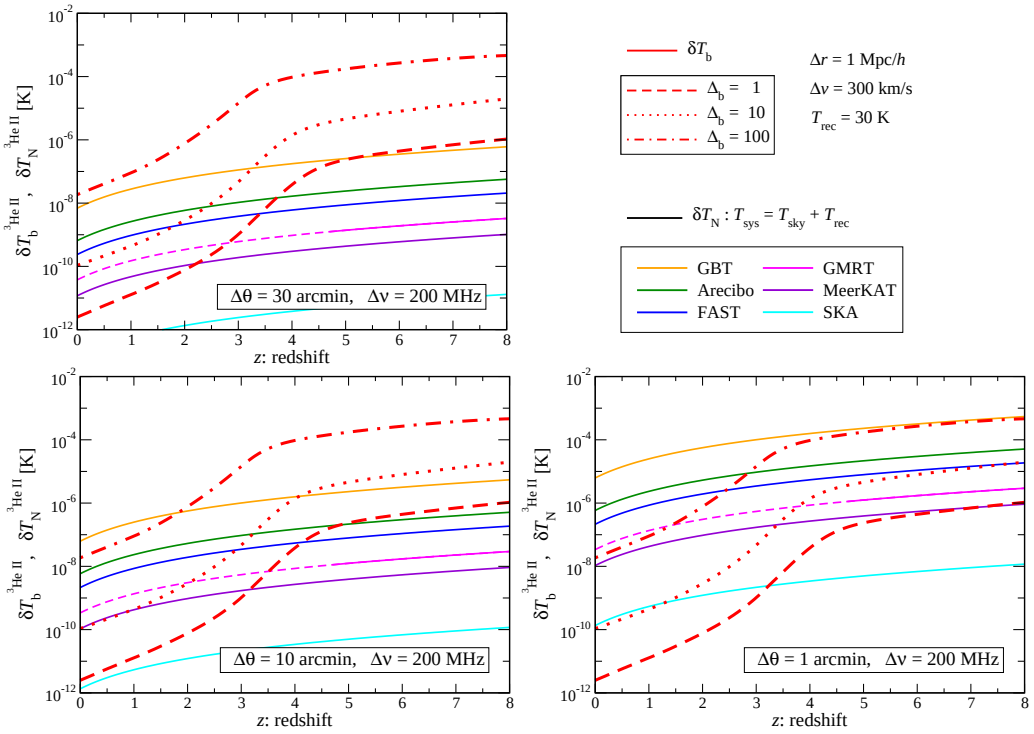

Figure 10. Same as the right panel in Figure 9, except the signals are the differential brightness temperature of ^{3}He II and the noise spectra are adopted for the observation at the rest frame frequency of 8.7 GHz. The frequency band width of $\Delta\nu = 200$ MHz, which corresponds to $\sim$100 Mpc/h width along the line-of-sight at $z = 0.5$, is adopted for all cases.

structure on the quasi-linear scales. In this paper we estimate the prospects for observing H I and ^{3}He II in the intergalactic filamentary structures using their respective hyperfine transitions.

The computation of the expected H I and ^{3}He II signal requires a precise estimation for the ionization state of each component and physical processes determining their spin temperatures. These calculations have been carried out assuming equilibrium radiative transport equations (Fukugita & Kawasaki 1994) and the UV/X-ray background model of Haardt & Madau (2012). Two types of filament models are considered: simple elongated slabs with varying baryon density, and filaments extracted from cosmologically simulated large scale filaments. The estimated signals of H I and ^{3}He II obtained are generally weak at low-redshifts. This is because hydrogen and helium reionization processes have both been completed. The amplitude of the brightness temperature of H I is $\delta T_{\rm b} \sim 10^{-6} - 10^{-3}$ K and of ^{3}He II is $\delta T_{\rm b} \sim 10^{-10} - 10^{-6}$K at $z = 0.5$. Even at $z = 1$, the signals of both H I and ^{3}He II increase only by a factor of a few.

We have also discussed whether current telescopes can reach the sensitivities required for observing H I and ^{3}He II emission from our filament models. Despite the low signal of H I, we have shown in this paper that these levels of sensitivity can be reached even by the present instruments, such as GBT, EVLA, and Arecibo with 100 hours of integration time. The ^{3}He II signal is much weaker than that of H I and is very hard to detect with present instruments. However, we show that detecting both H I and ^{3}He II from large scale filaments is possible with future telescopes, such as the full MeerKAT and SKA, given a reasonable amount of integration time.

At higher redshifts one benefits from larger signal, however, other issues start to become important. Most importantly, the beam size at higher frequencies becomes smaller, along with the field of view. The smaller beam size means that more distant filaments will not fill the beam, leading to a smaller detected signal. The field of view issue will limit the size of the filaments we can detect, especially if the filament is mostly elongated perpendicular to the line-of-sight. However, as we show the ^{3}He II signal around $z \sim 4$ is still in principle detectable even with the present instrument such as GMRT and Arecibo.

Obviously, one of the benefits of observing the two lines in the same filament is to give us a handle on the UV/X-ray background. In this work, we have adopted a single model for the background, but in future work this aspect will be explored in more detail.

In this paper we focus only on the direct detection of these signals. Less direct detections, e.g., statistical methods or cross-correlation approaches are also possible and, in some cases of H I been discussed by other authors (Chang et al. 2008). This is clearly an exciting route that promise to yield results in the foreseeable future. One can consider also detection of the signal in absorption towards background radio sources would be in principle advantageous to the emission signal at low

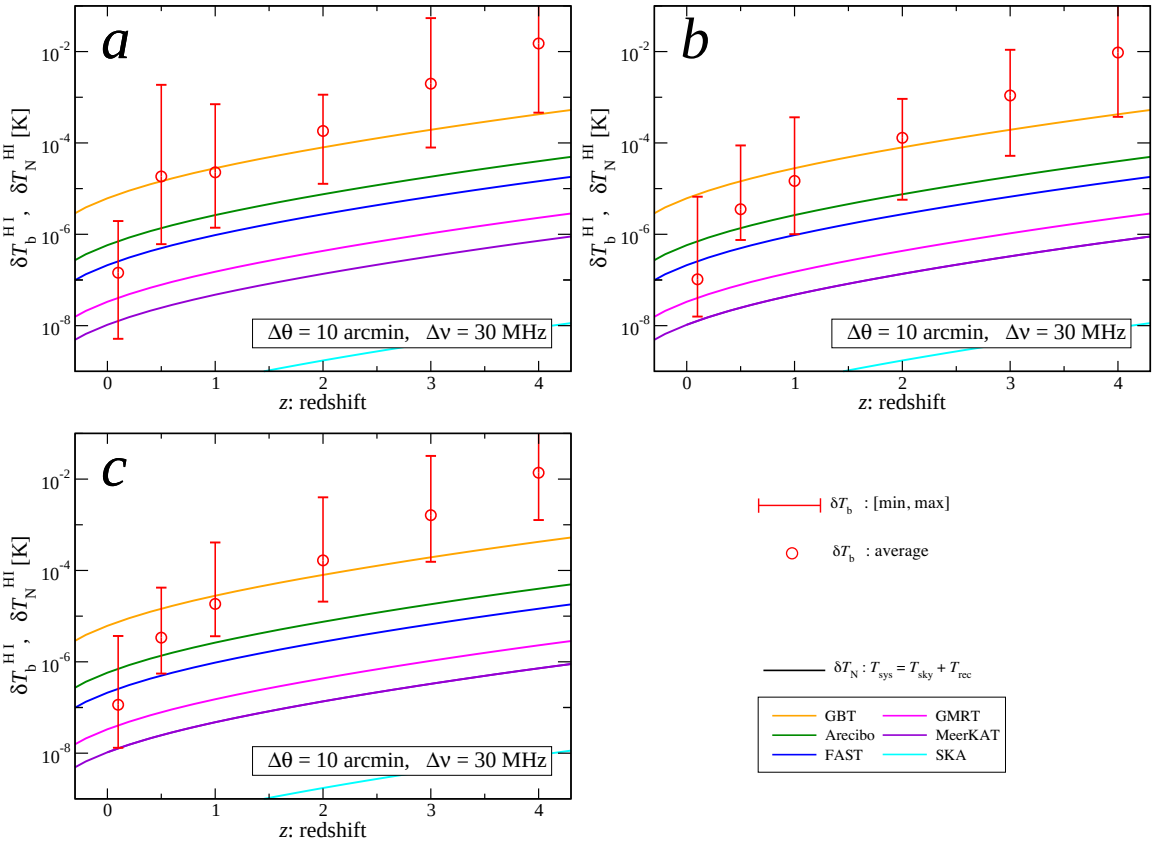

Figure 11. The redshift evolution of the H I signals from the filamentary structures labeled as a, b and c, and we show the results at $z = 0.1$, 0.5, 1, 2 and 4. Each data point represents the range of signal between maximum and minimum amplitudes, and the symbol represents the average value.

redshifts where the spin temperatures are low (McQuinn & Switzer 2009). This is of course depends on the number density of radio sources at high redshifts against which this measurement can be in principle done. We defer this to a future work.

It should be mentioned that we have not considered a number of effects that might make it more difficult to observe the signal, e.g., foregrounds, contamination from recombination lines, metal lines, etc. Fitting out the foregrounds will be necessary and the removing long wavelength modes along the line of sight is a crucial. This can be done provided that the bandwidth of the observation is much larger than the bandwidth covered by the filament. Such a requirement is easily satisfied with the current and future generations telescopes. In Addition, the point sources can also contaminate the observation, however these sources are very localized and can be removed by filtering them out using high angular resolution data, which is also available for current and future telescopes. These two issue will be dealt with in more detail in a future publication.

ACKNOWLEDGMENTS

We would like to thank A. G. de Bruyn for useful discussions and Elizabeth Fernandez for comments on the manuscript. We acknowledge support from JSPS (Japan Society for Promotion of Science) fellowship (YT); JSPS Grant-in-Aid for Scientific Research under Grants No. 25287057 (NS); Kobayashi-Maskawa Institute for the Origin of Particles and the Universe; and the World Premier International Research Center Initiative (WPI Initiative), MEXT, Japan. SZ acknowledges the Netherlands Organization for Scientific Research (NWO) VICI grant for financial support. This work was supported by the JSPS Strategic Young Researcher Overseas Visits Program for Accelerating Brain Circulation.

REFERENCES

Bagla J. S., Loeb A., 2009, ArXiv:0905.1698
Bell M. B., 2000, Astrophys. J, 531, 820

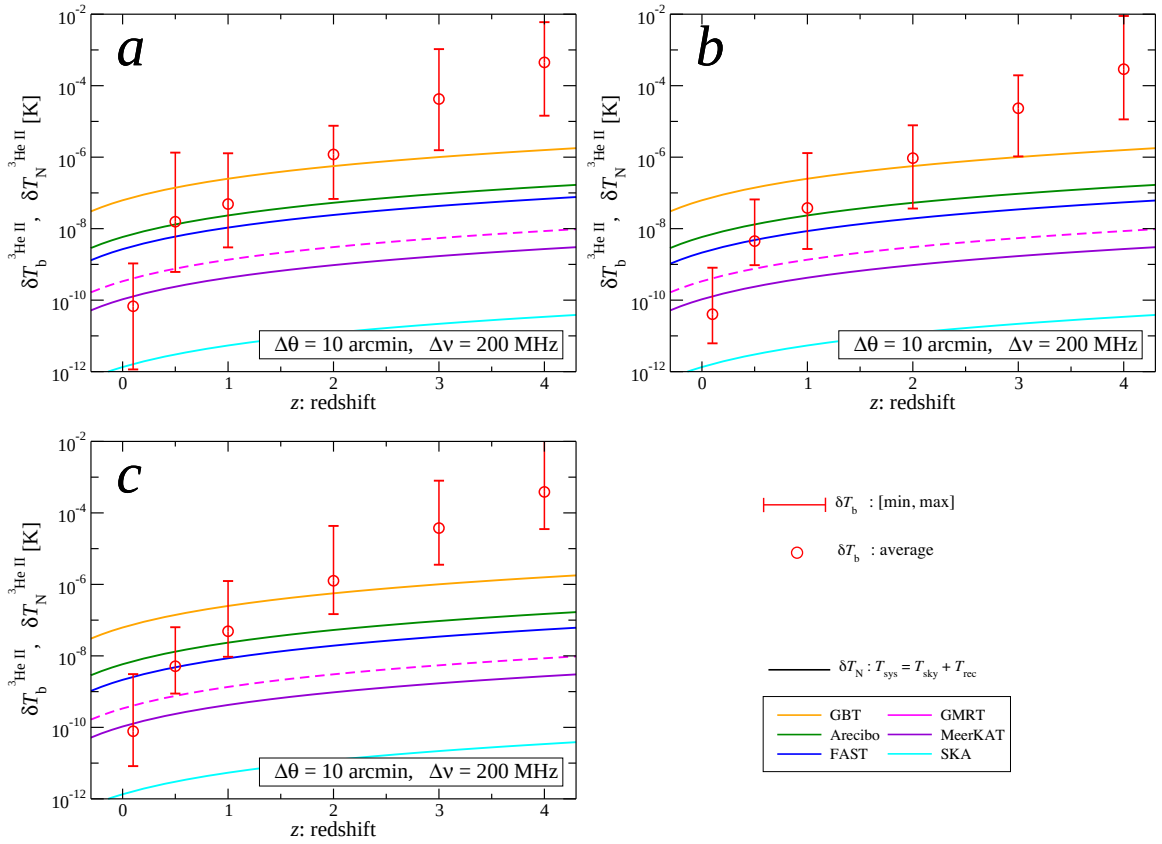

Figure 12. Same as Figure 11, but for the signal and sensitivity curves of ^{3}He II.

Bernardi G., de Bruyn A. G., Brentjens M. A., Ciardi B., Harker G., Jelić V., Koopmans L. V. E., Labropoulos P., Offringa A., Pandey V. N., Schaye J., Thomas R. M., Yatawatta S., Zaroubi S., 2009, Astron. & Astrophys., 500, 965

Bernardi G., de Bruyn A. G., Harker G., Brentjens M. A., Ciardi B., Jelić V., Koopmans L. V. E., Labropoulos P., Offringa A., Pandey V. N., Schaye J., Thomas R. M., Yatawatta S., Zaroubi S., 2010, Astron. & Astrophys., 522, A67

Black J. H., 1981, Mon. Not. R. Astron. Soc., 197, 553

Bond J. R., Kofman L., Pogosyan D., 1996, Nature, 380, 603

Cen R., 1992, Astrophys.J.Suppl., 78, 341

Cen R., Ostriker J. P., 1999, Astrophys. J, 514, 1

Chang T.-C., Pen U.-L., Bandura K., Peterson J. B., 2010, ArXiv:1007.3709

Chang T.-C., Pen U.-L., Peterson J. B., McDonald P., 2008, Physical Review Letters, 100, 091303

Chapman E., Abdalla F. B., Bobin J., Starck J.-L., Harker G., et al., 2012

Chapman E., Abdalla F. B., Bobin J., Starck J.-L., Harker G., Jelić V., Labropoulos P., Zaroubi S., Brentjens M. A., de Bruyn A. G., Koopmans L. V. E., 2013, Mon. Not. R. Astron. Soc., 429, 165

Choi E., Bond N. A., Strauss M. A., Coil A. L., Davis M., Willmer C. N. A., 2010, Mon. Not. R. Astron. Soc., 406, 320

Colless M., Dalton G., Maddox S., Sutherland W., Norberg P., Cole S., Bland-Hawthorn J., Bridges T., Cannon R., 2001, Mon. Not. R. Astron. Soc., 328, 1039

Erdoğdu P., Lahav O., Zaroubi S., Efstathiou G., Moody S., Peacock J. A., Colless M., Baldry I. K., Baugh C. M., Bland-Hawthorn J., 2004, Mon. Not. R. Astron. Soc., 352, 939

Ewen H. I., Purcell E. M., 1951, Nature, 168, 356

Field G. B., 1958, Proceedings of the IRE, 46, 240

Field G. B., 1959, Astrophys. J, 129, 536

Freudling W., Staveley-Smith L., Catinella B., Minchin R., Calabretta M., Momjian E., Zwaan M., Meyer M., O'Neil K., 2011, Astrophys. J, 727, 40

Fukugita M., Kawasaki M., 1994, Mon. Not. R. Astron. Soc., 269, 563

Fukugita M., Peebles P. J. E., 2004, Astrophys. J, 616, 643

Furlanetto S., Furlanetto M., 2007b, Mon.Not.Roy.Astron.Soc., 379, 130

Furlanetto S., Oh S. P., Briggs F., 2006, Phys.Rept., 433, 181
Furlanetto S. R., Furlanetto M. R., 2007a, Mon. Not. R. Astron. Soc., 374, 547
Furlanetto S. R., Oh S. P., Pierpaoli E., 2006, Phys.Rev., D74, 103502
Furlanetto S. R., Pritchard J. R., 2006, Mon. Not. R. Astron. Soc., 372, 1093
Goldwire Jr. H. C., Goss W. M., 1967, Astrophys. J, 149, 15
Gould R. J., 1994, Astrophys. J, 423, 522
Haardt F., Madau P., 2012, Astrophys. J, 746, 125
Harker G., Zaroubi S., Bernardi G., Brentjens M. A., de Bruyn A. G., Ciardi B., Jelić V., Koopmans L. V. E., Labropoulos P., Mellema G., Offringa A., Pandey V. N., Schaye J., Thomas R. M., Yatawatta S., 2009, Mon. Not. R. Astron. Soc., 397, 1138
Hirata C. M., 2006, Mon. Not. R. Astron. Soc., 367, 259
Jelić V., Zaroubi S., Labropoulos P., Bernardi G., de Bruyn A. G., Koopmans L. V. E., 2010, Mon. Not. R. Astron. Soc., 409, 1647
Jelić V., Zaroubi S., Labropoulos P., Thomas R. M., Bernardi G., Brentjens M. A., de Bruyn A. G., Ciardi B., Harker G., Koopmans L. V. E., b Pandey V. N., Schaye J., Yatawatta S., 2008, Mon. Not. R. Astron. Soc., 389, 1319
Kaiser N., 1987, Mon. Not. R. Astron. Soc., 227, 1
Komatsu E., Smith K. M., Dunkley J., Bennett C. L., Gold B., Hinshaw G., Jarosik N., Larson D., Nolta M. R., Page L., Spergel D. N., Halpern M., Hill R. S., Kogut A., Limon M., 2011, Astrophys. J Supp., 192, 18
McQuinn M., Switzer E. R., 2009, Phys.Rev., D80, 063010
Madau P., Meiksin A., Rees M. J., 1997, Astrophys. J, 475, 429
Masui K., Switzer E., Banavar N., Bandura K., Blake C., et al., 2012
Matsuda T., Sato H., Takeda H., 1971, Prog.Theor.Phys., 46, 416
Menzel D. H., Pekeris C. L., 1935, Mon. Not. R. Astron. Soc., 96, 77
Mo H., van den Bosch F., White S., 2010, Galaxy Formation and Evolution, 1 edn. Cambridge University Press
Muller C. A., Oort J. H., 1951, Nature, 168, 357
Nan R., Li D., Jin C., Wang Q., Zhu L., Zhu W., Zhang H., Yue Y., Qian L., 2011, International Journal of Modern Physics D, 20, 989
Nussbaumer H., Storey P. J., 1983, Astron. & Astrophys., 126, 75
Obreschkow D., Klöckner H.-R., Heywood I., Levrier F., Rawlings S., 2009, Astrophys. J, 703, 1890
Osterbrock D. E., 1989, Astrophysics of gaseous nebulae and active galactic nuclei
Pandey B., Kulkarni G., Bharadwaj S., Souradeep T., 2011, Mon. Not. R. Astron. Soc., 411, 332
Popping A., Braun R., 2011, Astron. & Astrophys., 527, A90
Popping A., Davé R., Braun R., Oppenheimer B. D., 2009, Astron. & Astrophys., 504, 15
Pritchard J. R., Furlanetto S. R., 2006, Mon. Not. R. Astron. Soc., 367, 1057
Pritchard J. R., Loeb A., 2012, Reports on Progress in Physics, 75, 086901
Rood R. T., Wilson T. L., Steigman G., 1979, Astrophys. J Lett., 227, L97
Shaver P. A., Windhorst R. A., Madau P., de Bruyn A. G., 1999, Astron. & Astrophys., 345, 380
Shchekinov Y. A., Vasiliev E., 2007, Mon.Not.Roy.Astron.Soc., 379, 1003
Sigurdson K., Furlanetto S. R., 2006, Physical Review Letters, 97, 091301
Skrutskie M. F., Cutri R. M., Stiening R., Weinberg M. D., Schneider S., Carpenter J. M., Beichman C., Capps R., Chester T., 2006, Astron. J., 131, 1163
Spitzer L., 1978, Physical Processes In The Interstellar Medium. Wiley classics library, Wiley & Son
Springel V., 2005, Mon. Not. R. Astron. Soc., 364, 1105
Sunyaev R. A., 1966, Astronomicheskii Zhurnal, 43, 1237
Switzer E. R., Masui K. W., Bandura K., Calin L.-M., Chang T.-C., Chen X.-L., Li Y.-C., Liao Y.-W., Natarajan A., Pen U.-L., Peterson J. B., Shaw J. R., Voytek T. C., 2013, ArXiv:1304.3712
Tempel E., Stoica R. S., Martínez V. J., Liivamägi L. J., Castellan G., Saar E., 2014, Mon. Not. R. Astron. Soc., 438, 3465
Townes C. H., 1957, in van de Hulst H. C., ed., Radio astronomy Vol. 4 of IAU Symposium, Microwave and radio-frequency resonance lines of interest to radio astronomy. p. 92
van de Hulst H., 1945, Nederlands Tijdschrift voor Natuuurkunde, 11, 210
van Haarlem M. P., Wise M. W., Gunst et al. 2013, Astron. & Astrophys., 556, A2
Verner D. A., Ferland G. J., 1996, Astrophys. J Supp., 103, 467
Wouthuysen S. A., 1952, Astron. J., 57, 31
York D. G., Adelman J., Anderson Jr. J. E., SDSS Collaboration 2000, Astron. J., 120, 1579
Zaroubi S., 2013, in Wiklind T., Mobasher B., Bromm V., eds, Astrophysics and Space Science Library Vol. 396 of Astrophysics and Space Science Library, The Epoch of Reionization. p. 45
Zygelman B., 2005, Astrophys. J, 622, 1356

APPENDIX A: RECOMBINATION AND IONIZATION COEFFICIENTS

For the sake of completeness, here we summarize the recombination and collisional ionization rates and the cooling function adopted in this work. We take these values from Fukugita & Kawasaki (1994); Mo et al. (2010). Similar expressions also can be found in Menzel & Pekeris (1935); Matsuda et al. (1971); Spitzer (1978); Black (1981); Cen (1992); Verner & Ferland (1996).

A1 Recombination and Collisional ionization rates

Collisional ionization

H I $\rightarrow$ H II :

$$\beta_{\rm HI} = 5.85\times10^{-11}T^{1/2}\left(1+T_5^{1/2}\right)^{-1}\exp(-1.578/T_5)\ {\rm cm}^3\cdot{\rm sec}^{-1}\,. \tag{A1}$$

He I $\rightarrow$ He II :

$$\beta_{\rm HeI} = 2.38\times10^{-11}T^{1/2}\left(1+T_5^{1/2}\right)^{-1}\exp(-2.853/T_5)\ {\rm cm}^3\cdot{\rm sec}^{-1}\,. \tag{A2}$$

He II $\rightarrow$ He III :

$$\beta_{\rm HeII} = 5.68\times10^{-12}T^{1/2}\left(1+T_5^{1/2}\right)^{-1}\exp(-6.315/T_5)\ {\rm cm}^3\cdot{\rm sec}^{-1}\,. \tag{A3}$$

Recombination

H II $\rightarrow$ H I : (free $\rightarrow n\geqslant 1$)

$$\alpha_{\rm HII} = 3.96\times10^{-13}T_4^{-0.7}\left(1+T_6^{0.7}\right)^{-1}\ {\rm cm}^3\cdot{\rm sec}^{-1}\,. \tag{A4}$$

He II$\rightarrow$ He I : (free $\rightarrow n\geqslant 1$)

$$\alpha_{\rm HeII} = 4.31\times10^{-10}T_4^{-0.6353}\ {\rm cm}^3\cdot{\rm sec}^{-1}\,. \tag{A5}$$

He III$\rightarrow$ He II : (free $\rightarrow n\geqslant 1$)

$$\alpha_{\rm HeIII} = 2.12\times10^{-12}T_4^{-0.7}\left(1+0.379T_6^{0.7}\right)^{-1}\ {\rm cm}^3\cdot{\rm sec}^{-1}\,. \tag{A6}$$

Dielectric recombination

He II $\rightarrow$ He I : (dielectric recombination) (Nussbaumer & Storey 1983; Osterbrock 1989)

$$\xi_{\rm HeII} = 6.0\times10^{-10}T_5^{-1.5}\exp(-4.7/T_5)\left[1+0.3\exp(-0.94/T_5)\right]\ {\rm cm}^3\cdot{\rm sec}^{-1}\,. \tag{A7}$$

A2 Cooling function

We define the cooling function Λ as;

$$\Lambda = \sum_{i={\rm HI,HeI,HeII}}\zeta_i n_e n_i \ + \sum_{i={\rm HI,HeI,HeII}}\psi_i n_e n_i \ + \sum_{i={\rm HII,HeII,HeIII}}\eta_i n_e n_i \ + \ \omega_{\rm HeII}n_e n_{\rm HeIII} \ + \ \lambda_{\rm c} \ + \ \theta_{\rm ff}(n_{\rm HII}+n_{\rm HeII}+4n_{\rm HeIII})n_e\,, \tag{A8}$$

where the right hand side terms are the collisional-ionization cooling, the collisional excitation cooling, the recombination cooling, the dielectron recombination cooling, the Compton cooling and the free-free cooling, respectively. The symbols ζ_i, ψ_i, η_i, and ω_i represent the cooling coefficients due to atomic state i, $\lambda_{\rm c}$ is the Compton cooling rate, and $\theta_{\rm ff}$ is the free-free cooling coefficient. We summarize the detail expressions of these values below.

Collisional ionization cooling

H I :

$$\zeta_{\rm HI} = 1.27\times10^{-21}T^{1/2}\left(1+T_5^{1/2}\right)^{-1}\exp(-1.58/T_5)\ {\rm erg}\cdot{\rm cm}^3\cdot{\rm sec}^{-1}\,. \tag{A9}$$

He I :

$$\zeta_{\rm HeI} = 9.38\times10^{-22}T^{1/2}\left(1+T_5^{1/2}\right)^{-1}\exp(-2.85/T_5)\ {\rm erg}\cdot{\rm cm}^3\cdot{\rm sec}^{-1}\,. \tag{A10}$$

He I (2^3S) :

$$\zeta_{\rm HeI,2^3S} = 5.01\times10^{-27}T^{-0.1687}\left(1+T_5^{1/2}\right)^{-1}\exp(-5.53/T_4)n_e n_{\rm HeII}/n_{\rm HeI}\ {\rm erg\cdot cm^3\cdot sec^{-1}}\,. \tag{A11}$$

He II :

$$\zeta_{\rm HeII} = 4.95\times10^{-22}T^{1/2}\left(1+T_5^{1/2}\right)^{-1}\exp(-6.31/T_5)\ {\rm erg\cdot cm^3\cdot sec^{-1}}\,. \tag{A12}$$

Collisional excitation cooling

H I :

$$\psi_{\rm HI} = 7.5\times10^{-19}\left(1+T_5^{1/2}\right)^{-1}\exp(-1.18/T_5)\ {\rm erg\cdot cm^3\cdot sec^{-1}}\,. \tag{A13}$$

He I :

$$\psi_{\rm HeI} = 9.10\times10^{-27}T^{-0.1687}\left(1+T_5^{1/2}\right)^{-1}\exp(-1.31/T_4)n_e n_{\rm HeII}/n_{\rm HeI}\ {\rm erg\cdot cm^3\cdot sec^{-1}}\,. \tag{A14}$$

He II :

$$\psi_{\rm HeII} = 5.54\times10^{-17}T^{-0.397}\left(1+T_5^{1/2}\right)^{-1}\exp(-4.73/T_5)\ {\rm erg\cdot cm^3\cdot sec^{-1}}\,. \tag{A15}$$

Recombination cooling

H II :

$$\eta_{\rm HII} = 2.82\times10^{-26}T_3^{0.3}\,(1+3.54T_6)^{-1}\ {\rm erg\cdot cm^3\cdot sec^{-1}}\,. \tag{A16}$$

He II :

$$\eta_{\rm HeII} = 1.55\times10^{-26}T^{0.3647}\ {\rm erg\cdot cm^3\cdot sec^{-1}}\,. \tag{A17}$$

He III :

$$\eta_{\rm HeIII} = 1.49\times10^{-25}T^{0.3}\,(1+0.885T_6)^{-1}\ {\rm erg\cdot cm^3\cdot sec^{-1}}\,. \tag{A18}$$

Dielectronic recombination cooling

He II :

$$\omega_{\rm HeII} = 1.24\times10^{-13}T^{-1.5}\,(1+0.3\exp(-9.4/T_4))^{-1}\exp(-4.7/T_5)\ {\rm erg\cdot cm^3\cdot sec^{-1}}\,. \tag{A19}$$

Free-free cooling

$$\theta_{\rm ff} = 1.42\times10^{-27}g_{\rm ff}T^{1/2}\,, \tag{A20}$$

where $g_{\rm ff}$ is the mean Gaunt factor and the values of $g_{\rm ff}$ are between 1.1 and 1.5 for $T = 10^4$-10^8 K (Spitzer 1978) and we adopt the value of $g_{\rm ff} = 1.1$ in this paper.

Compton cooling

$$\lambda_{\rm c} = 4k_{\rm B}(T-T_\gamma)\frac{\pi^2}{15}\left(\frac{k_{\rm B}T_\gamma}{\hbar c}\right)^3\left(\frac{k_{\rm B}T_\gamma}{m_e c^2}\right)n_e\sigma_{\rm T}c\,. \tag{A21}$$

APPENDIX B: THE COMOVING DISTANCE FOR A GIVEN BANDWIDTH

The comoving spatial size $r_{\rm A}$ and the depth along the line-of-sight Δr for an observation depend on the cosmological model. We here summarize them and their relationship with the survey parameters.

When the angular resolution θ_s is given, the spatial size can be determined by

$$r_{\rm A} = \theta_s\chi(z)\,, \tag{B1}$$

where $\chi(z)$ is the comoving distance to the observed source at redshift z. On the other hand, the depth along the line-of-sight is determined by the frequency band width $\Delta\nu$ and the relationship between them is given by

$$\frac{\Delta r}{\Delta\nu} \simeq \frac{1+z}{\nu_0}\frac{c}{H(a)}\,, \tag{B2}$$

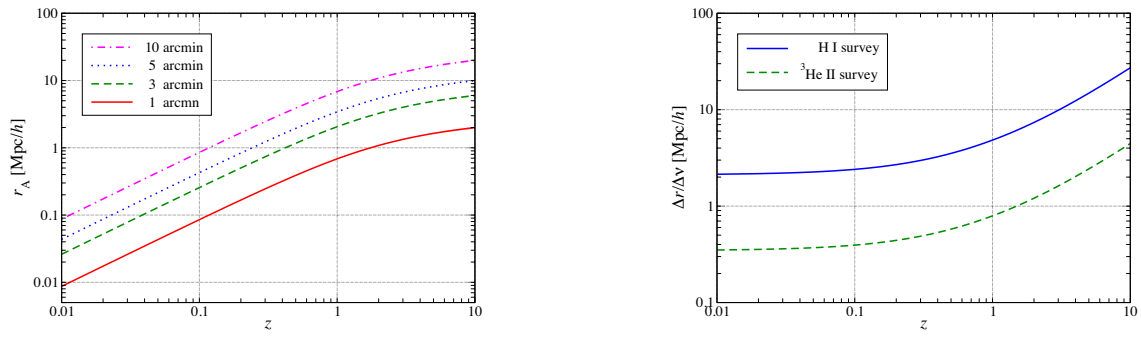

Figure A1. (Left)The spacial size $r_{\rm A}$ with different values of the angular size θ_s as a function of redshift. (Right)The relationship between the frequency band width $\Delta\nu$ and the spacial length along the line-of-sight Δr for the H I (solid-line) and the ^{3}He II (dashed-line) observations, respectively.

where $\Delta\nu$ is the frequency bandwidth and ν_0 is the rest-frame frequency of the observed source. Therefore this relationship differs between the H I and ^{3}He II observations.

We show the results with our cosmological model as a function of redshift in Figure A1.

This paper has been typeset from a TEX/ LATEX file prepared by the author.